ENHANCED VERTICAL MIXING WITHIN MESOSCALE EDDIES DUE TO HIGH FREQUENCY WINDS IN THE SOUTH CHINA SEA

A Thesis
Presented to
The Academic Faculty

by

Yuley Mildrey Cardona Orozco

In Partial Fulfillment
of the Requirements for the Degree
Master in Earth and Atmospheric Sciences in the
School of Earth and Atmospheric Sciences

Georgia Institute of Technology
August 2011

ENHANCED VERTICAL MIXING WITHIN MESOSCALE EDDIES DUE TO HIGH FREQUENCY WINDS IN THE SOUTH CHINA SEA

Approved by:

Dr. Annalisa Bracco, Advisor
School of Earth and Atmospheric Sciences
Georgia Institute of Technology

Dr. Emanuele Di Lorenzo
School of Earth and Atmospheric Sciences
Georgia Institute of Technology

Dr. Yi Deng
School of Earth and Atmospheric Sciences
Georgia Institute of Technology

TABLE OF CONTENTS

LIST OF TABLES

LIST OF FIGURES

SUMMARY

The South China Sea is a marginal basin with a complex circulation influenced by the East Asian Monsoon, river discharge and intricate bathymetry. As a result, both the mesoscale eddy field and the near-inertial energy distribution display large spatial variability and they strongly influence the oceanic transport and mixing.

With an ensemble of numerical integrations using a regional ocean model, this work investigates how the temporal resolution of the atmospheric forcing fields modifies the horizontal and vertical velocity patterns and impacts the transport properties in the basin. The response of the mesoscale circulation in the South China Sea is investigated under three different forcing conditions: monthly, daily and six-hourly momentum and heat fluxes. While the horizontal circulation does not display significant differences, the representation of the vertical velocity field displays high sensitivity to the frequency of the wind forcing. If the wind field contains energy at the inertial frequency or higher (daily and six-hourly cases), then Vortex Rossby waves and near inertial waves are excited as ageostrophic expression of the vigorous eddy field. Those waves dominate the vertical velocity field in the mixed layer (vortex Rossby waves) and below the first hundred meters (near inertial waves) and they are responsible for the differences in the vertical transport properties under the various forcing fields as quantified by frequency spectra, vertical velocity profiles and vertical dispersion of Lagrangian tracers.

CHAPTER 1. INTRODUCTION

The dynamics of the ocean mesoscale, between about 10 and 500 km, is generally approximated as that of a stably stratified, rapidly rotating flow in the geostrophic, hydrostatic approximation. Horizontal velocities are much larger than the vertical ones, and the motion is approximately two-dimensional and characterized by the presence of coherent vortices or eddies (Provenzale, 1999). Those eddies concentrate energy and vorticity (McWilliams, 1984, 1990), represent dynamical anomalies in variables such as velocity, sea surface height and density (Klein and Lapyre, 2009) and are fundamental to the horizontal and vertical transport processes and to the statistical properties of the turbulence field (Bracco et al., 2000; Bracco and McWilliams, 2010; Capet et al., 2008; Stammer, 1997). They play a crucial role in the transport of ocean heat and momentum; they impact the local dynamics with important consequences on tracer dispersion, ocean stirring and mixing processes (Pasquero et al., 2007); and they affect the biology of the ocean and the nutrients distribution (Abraham, 1998; Bracco et al., 2009; Lévy and Klein, 2004; Martin and Richards, 2001;McGillicuddy et al., 1997; Pasquero et al., 2005). Finally they contribute substantially to the dissipation of energy introduced by the wind forcing (Munk and Wunch, 1998; Wunsch and Ferrari, 2004) that transfers atmospheric kinetic energy into oceanic kinetic and potential energies (Lueck and Reid, 1984).

Most of this wind energy is trapped at the ocean surface and contributes to the turbulent mixing in the mixed layer (Wunsch and Ferrari, 2004). Part of it, however, can propagate to the ocean interior by mean of internal wave motion and is distributed at different periods and vertical scales (Kundu, 1976; Kunze, 1985;Pollard and Millard, 1970). Vertical shear can then propitiate wave breaking and enhance mixing (Garret, 2003). In the ocean eddies contribute to this energy transfer towards the dissipation scale by effectively polarizing quasi- and near-inertial motions.

For quasi-inertial processes here we refer to the development of vortex Rossby waves (VRWs) in eddies. The term was used for the first time by McDonald (1968) and a quantitative description of the VRWs behavior can be found in Montgomery & Kallenback (1997). Using a shallow water model, McWilliams et al. (2003) and Graves et al. (2006) introduced them to the oceanographic community to explain the physical mechanism by which anticyclone are predominant in ocean interior, commonly known as anticyclone/cyclone asymmetry. VRWs result from vortex-mean flow interactions and they owe their existence to the finite radial gradient of potential vorticity in coherent eddies and are excited by the shear deformation of the mean potential vorticity of the eddies by the background flow. Vorticity perturbations in monopolar vortices propagate outward as VRWs, shared away by the angular velocity of the mean axisymmetric vortex. Koszalka et al. (2009) investigated for the first time their formation and structure using a regional ocean model in an idealized configuration and Chavanne et al. (2010) documented their existence in a cyclone observed west of Oahu, Hawaii, using high-frequency radio Doppler current meters and moored acoustic Doppler current profilers (ADCPs).

Near-inertial waves (NIWs) in eddies, on the other hand, have been studied and observed extensively by the oceanographic community. They are trapped within the anticyclonic structures while expelled from the cyclonic ones, as shown by a number of theoretical and idealized numerical studies (Danioux et al., 2008; Koszalka et al., 2009, 2010; Kunze 1985, Lee and Niiler, 1998; to cite a few). The first observational evidence of this behavior has been found in the North Pacific and in the Sargasso Sea, where downward propagating near inertial energy was observed in regions of negative vorticity by Kunze and Sanford (1984; 1986). More recent examples include satellite-tracked drifter observations over the Kuril-Kamchatka Trench (Rabinovich et al., 2002; Rogachev and Carmack, 2002) and moored current observations in the

southwestern East/Japan Sea (Byun et al., 2010). As a consequence vertical mixing induced by the inertial energy is heterogeneous and strongly related to the eddy field properties (Klein et al, 2004; Koszalka et al., 2010).

This heterogeneity makes it difficult to map and measure the overall contribution of quasi- and near- inertial waves trapped in eddies on the oceanic vertical mixing and energy dissipation processes. Numerical simulations with state-of-the-art ocean general circulation models may provide a leading order answer (Zhai et al., 2007). Within a modeling framework, however, the frequency of the wind forcing affects the production of NIWs. Indeed, near-inertial motions are effectively excited only by high (with respect to the Coriolis frequency f) frequency (HF) winds as the interaction between winds and NIWs results from a resonance mechanism or 'ringing of the eddy field' (Danioux and Klein, 2008; Klein et al., 2004; Large and Crawford, 1995; Skyllingstadt et al., 2000).

Several studies performed in the last few years using numerical models in idealized domains investigated the interaction between the NIW field and the eddy field at the meso- and sub-mesoscale (Danioux et al., 2008; Klein et al., 2004; Komori et al., 2008; Koszalka et al., 2009; Zhai et al., 2005). Here we test those results in a realistic domain, using the Regional Ocean Modeling System (ROMS) configured in the South China Sea (SCS) and forced by reanalysis winds and heat fluxes at monthly, daily and six hourly frequency for the period 2000 - 2007. Our goal is evaluate how the use of wind products containing high (i.e. daily and 6-hourly) frequencies changes the modeled fields and the associated mixing, and the representation of quasi- and near-inertial processes in ROMS. We focus in particular on the horizontal and vertical transport.

The choice of the SCS as model domain is motivated by two reasons. First of all, the SCS is an enclosed basin with complex dynamics influenced by the East Asian Monsoon and intricate bathymetry, that together lead to a large temporal and spatial variability on the mesoscale eddy field and to the generation of an intense internal wave field over the rough topography. This peculiarity allows us to evaluate the relative role of the HF winds-induced and topographically-induced wave fields on the vertical and horizontal mixing. Secondly, the SCS is located in the tropics and the Coriolis period is relatively long (1.9 day). Both daily and 6-hourly winds contain energy at the frequencies required to 'ring the eddies'.

The next chapter presents the experiment setup and model validation over SCS domain. chapter 3 briefly describes the relative role of HF winds and heat fluxes. Chapter 4 focuses on the role of HF winds on the model representation of the mesoscale eddy field and the associated horizontal transport; chapter 5 discusses how HF winds modify the eddy contribution to the vertical transport and mixing. Conclusions follow in chapter 6.

CHAPTER 2. THE OCEAN NUMERICAL MODEL

The SCS is a semi-enclosed ocean basin bounded by the East China Sea to the northeast, the Pacific Ocean and the Sulu Sea to the east, and the Java Sea and the Indian Ocean to the southwest. In the south the SCS has a broad continental shelf where the water depth reaches at most 200 m, while in the north it is characterized by very deep waters (greater than 3000 m). Figure 1 displays the intricate bathymetry.

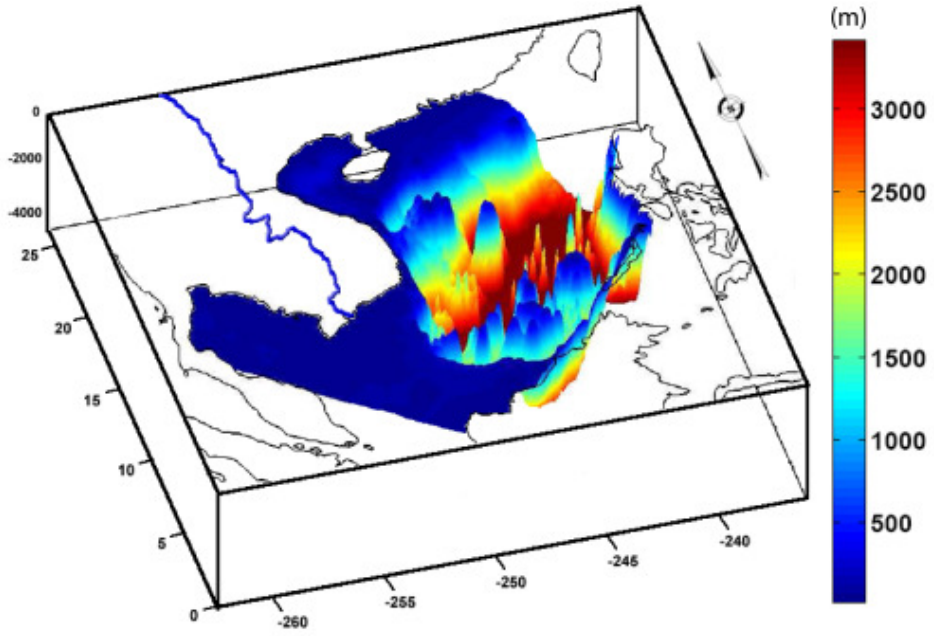

Figure 1. Bathymetry of the SCS adopted in all simulations. Data from ETOPO2

In this work we use the Regional Ocean Modeling System (ROMS) in the domain delimited by 1° N - 22° N and 98° E - 122° E. ROMS is an incompressible, free-surface, hydrostatic, eddy-resolving primitive equation model that uses stretched, terrain-following coordinates (s-coordinates) in the vertical and orthogonal curvilinear coordinates in the

horizontal (Shchepetkin and McWilliams, 2005). It use the K-profile parameterization (KPP) scheme for vertical mixing (Large et al., 1994) and implicit horizontal mixing associated with the third-order upstream bias scheme (Shchepetkin and McWilliams, 1998).

The model grid for the SCS has a horizontal resolution of 5 km and 20 vertical terrain following s-layers, with at least seven layers in the upper 400 m. The model bathymetry is derived from the digital data base of land and sea-floor elevations on a 2-minute latitude/longitude grid (ETOPO2). The bathymetry is smoothed to reduce pressure gradient errors and the minimum water depth is set to 20 m. Open boundaries are prescribed in the north, east and south and closed boundaries are used in the west. At the open lateral boundary an active, implicit, upstream-biased radiation condition (Marchesiello et al., 2001) connects the model solution to SODA (Simple Ocean Data Assimilation reanalysis; Carton and Giese, 2008). First of all, we run a ten year long integration forced by climatological atmospheric fields and boundary conditions and initialized using SODA temperature, salinity, velocities and sea surface high (SSH). This equilibrated ROMS solution is then used to initialize the integrations described in this work. We run three simulations using wind stress fields from the NCEP/QUICKSCAT blended ocean winds from Colorado Research Associates (version 5.0) (Millif, et al., 2004 and Chin et al., 1998) and net surface heat, freshwater and shortwave radiation fluxes derived from the US National Center for Environmental Prediction (NCEP) (Kistler et al., 2001) at monthly (Mon in the following), daily (Day) and six hourly (6h) temporal resolution. In all integrations the NCEP surface heat fluxes are corrected, in all runs, using NOAA extended SST (Smith and Reynolds, 2003) at a resolution of 2×2 degrees. This correction, with time-scale of one month, avoids long-term drifts in the SST climatology associated with errors in the NCEP surface fluxes (Josey, 2001) and is standard practice in the regional modeling community. No tidal forcing is

applied. All runs cover 2000-2007 (see Table 1) and the period 2001-2007 is considered in our analysis (the first year being discarded as model adjustment to the new forcing fields).

To quantify the impact of HF atmospheric forcing on the horizontal and vertical transport in the SCS eddy field we also deploy Lagrangian tracers. The equation $\frac{d\vec{x}}{dt} = \vec{u}(\vec{x}, t)$, where $\vec{x}$ is the Lagrangian particle position vector and $\vec{u}$ is the Eulerian velocity vector interpolated at the particle location, is integrated using 4^{th} order Milne predictor and 4^{th} order Hamming corrector scheme. 8192 particles are released at 20 m and at 1000 m depth over areas where the bottom is deeper than 3000 m to limit the influence of internal waves generated by interactions of the current with the bottom roughness. The particles, deployed on January, 10^{th} 2005 are tracked for 50 days and their positions and velocities are recorded every two hours. By the end of February 7% of the particles deployed have left the domain through the open boundaries and their trajectories have been discarded in the analysis.

Table 1. Configuration of the atmospheric forcing fields for the six integrations analyzed in this work

Fluxes Wind	*Mon*	*Day*	*6h*
Mon	Mon-*Mon*		
Day	Day-*Mon*	Day-*Day*	
6h	6h-*Mon*	6h-*Day*	6h-*6h*

2.1 Model Climatology

The circulation in the SCS is modulated by the Western North Pacific East Asian monsoon (WNPM) (Fang et al., 2003; Hu et al., 2000; Lau et al., 1998; Metzger, 2003; Qu,

2000; Wang et al., 2006; Wei et al., 2003; Wu et al., 1998; Wyrtki, 1974; Xue et al., 2004;). During the winter monsoon season (November to March), winds are northeasterly and the wind stress reaches values around 0.3 N/m^2. The circulation is dominated by two cyclonic gyres and by intensified boundary currents along the western boundary of the basin that result in a southward coastal jet off the coast. Conversely, in the summer monsoon season (May to August), southwesterly winds result in a momentum stress barely exceeding 0.1 N/m^2 on average over the basin (Chu and Li, 2000). This wind stress generates a northward coastal jet off the coast of Vietnam and an anticyclonic gyre in the south. The interaction of the coastal jet with the bathymetry contributes to the offshore transport of Mekong waters to the basin interior with the formation of coherent eddies entraining some of the river waters (SODA includes seasonal river discharge information from the World Meteorological Organization). Figure 2 displays the SSH anomalies and geostrophic currents fields derived from the AVISO satellite data-set and in the model output for December to February (DJF) and June to August (JJA), averaged over the integration period 2001-2007. Overall, the model captures well the mean circulation patterns, with a modest overestimation of the strength of the cyclonic recirculation zone in the south in boreal winter and an underestimation of the anticyclonic gyre in the north in summer. The correlation between ssh seasonal cycle anomalies from AVISO and the model output runs is between 0.87 and 0.91. No significant differences are found in the mean surface circulation between the simulation forced by monthly averaged winds (panels c and d), and the Day (not shown) or 6h run (panels e and f). The horizontal circulation at depth is also analogous in all integrations performed (not shown). The interannual variability is well simulated by ROMS and no significant differences are seen between the various runs, but is not discussed here being irrelevant for the focus of this work.

CHAPTER 3. TEMPORAL RESOLUTION OF THE ATMOSPHERIC FORCING

With a set of runs we investigate the impact of varying temporal resolution of the atmospheric heat and momentum forcings. The goal is to describe how the modeled circulation responds to increasing the atmospheric forcing frequency from monthly to six-hourly focusing on the transport processes. All forcing fields are further linearly interpolated to ROMS time step, which is 240 seconds in our simulations. Three runs, analyzed throughout this work, make use of equal temporal resolution for wind and heat fluxes respectively, and are indicated in Table 1 as Mon-*Mon*, Day-*Day* and 6h-*6h*. We also performed a second group of sensitivity integrations to verify that our conclusions depended primarily on the HF wind contribution as already shown for the SCS by (Fan et al., 2010) by maintaining six hourly wind forcing and using monthly-, daily- or 6-hourly varying heat fluxes (6h-*Mon* and 6h-*Day*, to be considered together with 6h-*6h*).

Overall the average circulation measured in terms of eddy kinetic energy, horizontal velocity and vorticity fields, and sea surface height does not vary between runs (see for example Figure 2 and Figure 6), it is confirmed by the correlation between the ssh seasonal anomalies calculated from AVISO and the model simulations listed in table1, the correlations are high in all cases (over 0.85) and close between them. In this respect the SCS differs from other basins, e.g. the Black Sea (Kara et al., 2005) or the Ligurian Sea (Casella et al., 2011), where high frequency atmospheric forcing has a direct impact on the strength of the coastal currents and on the eddy formation processes. The physical reason resides in the key role that the steep and complicated topography exerts in determining the mesoscale dynamics of the SCS. Eddies predominately

form where the currents impinge over the rough topography and then propagate into deeper waters populating the basin interior.

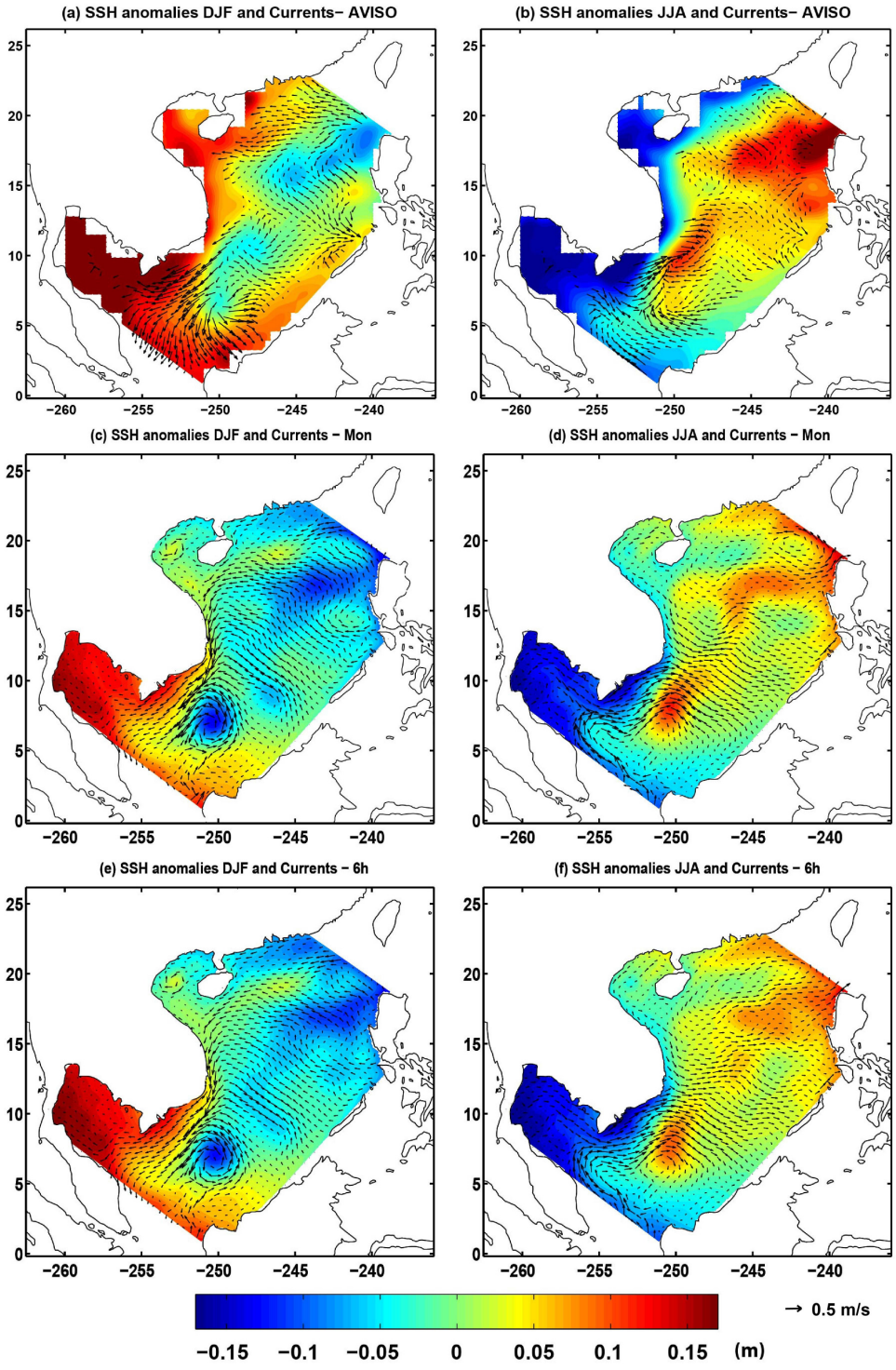

Figure 2. SSH anomalies (m) and geostropic currents in boreal winter (DJF, left) and summer (JJA, right). Observations from OI.V2 and AVISO (a) (b), Model output Mon-Mon run (c) (d) and Model Output 6h-6h run (e) (f).

The temperature, salinity and density fields, however, depend on the temporal resolution of the atmospheric forcing fields. Figure 3 shows the mean temperature profiles for the two groups of runs described above, together with the ones derived from SODA and from the ORA-S3 ECMWF (Balmaseda et al., 2008) ocean reanalysis for the boreal winter and summer seasons. The profiles are calculated over a sub-domain with depth greater than 500 m, removing the very shallow areas in the south. Independently on the run, the model main thermocline is shallower and less sharp than the one of SODA or ORA-S3 reanalysis. Focusing on the top panels, differences are evident through the whole water column, whenever momentum and heat fluxes frequency increases from monthly to six hourly. In winter in the upper 30-40 m, the modeled profiles are all characterized by colder temperatures than SODA and on average in good agreement with ORA-S3. Day-*Day* and 6h-6h display a significant temperature decrease compared to Mon-*Mon*, up to 0.3 degrees on average over the whole domain and up to 1 degrees in locations where the bathymetry is predominately flat (see for example in Figure 4), due to enhanced mixing of surface warm waters within the mixed layer, in agreement with similar studies in the Pacific (Fan et al, 2010, Chen et al., 1999; Lee and Liu, 2005 and Sui et al., 2003) and Southern Ocean in austral summer (Kamenkovich, 2005). Immediately below the mixed layer (~ 35 m) the differences between the three runs decrease. Compared to reanalsysis, the modeled temperatures appear all colder than SODA by approximately 2^{o}C but with similar gradients for increasing depth, and very different from ORA-S3 (up to 5 ^{o}C colder). The mean temperatures associated with Daily and 6-hourly fluxes are now slightly warmer than the ones for monthly fluxes and this behavior continues until ~200 m depth, in agreement with the results

presented by Sui et al., (2003) for the tropical Pacific and Ezer, (2000) over the North Atlantic. A cooling trend for increasing frequency of the atmospheric fluxes is noticeable below the main thermocline; it is due to the enhanced mixing of the deeper water column induced by high frequency winds, as we will further show in the remaining of the work. As a result, the stratification in the Day-*Day* and 6h-*6h* runs is in closer agreement with SODA and ORA-S3 reanalysis than Mon-*Mon* (below the main thermocline the two reanalysis data-sets are nearly indistinguishable). In boreal summer the behavior is similar to the one described for winter, with less pronounced differences at the surface, but a diffuse cooling of similar amplitude below the main thermocline.

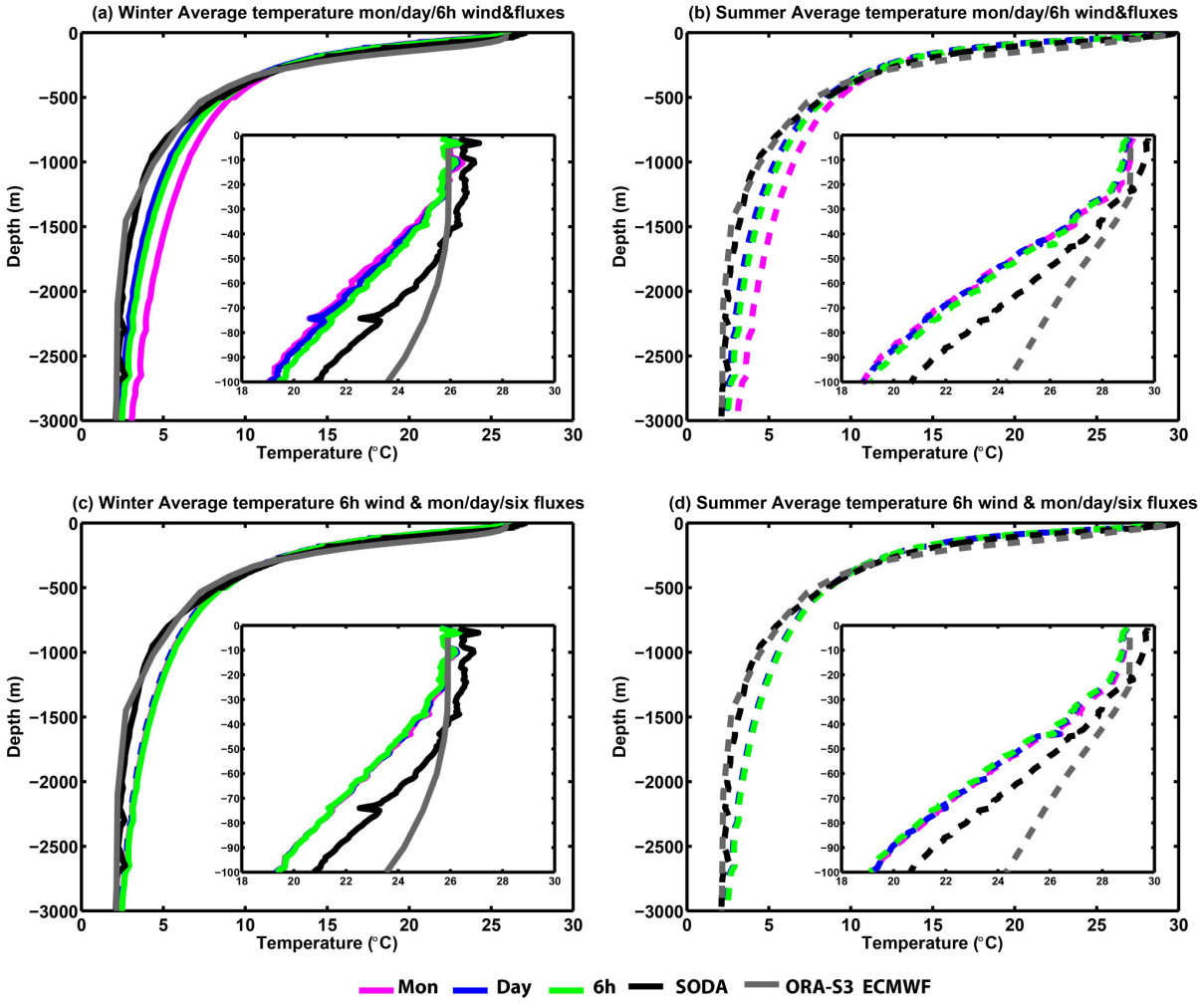

Figure 3. Mean temperature profile in ºC in boreal winter (DJF, left) and summer (JJA, right) for (a) (b) Mon-*Mon*, Day-*Day*, 6h-*6h*, SODA and ORA-S3; and (c), (d) 6h-*Mon*, 6h-*Day* and 6h-*6h*, SODA and ORA-S3. In all panels the insets show a zoom over the first 100 m of the water column.

The general trend from Mon-*Mon* to 6h-*6h* integrations described above is enhanced in the temperature differences shown in Figure 4 for a vertical section running across the basin (its location is marked in Figure 5 in black). This section, chosen for the high level of eddy activity and deep waters, displays the mean temperature differences between Day-*Day* or 6h-*6h* and Mon-*Mon* during boreal winter and summer in the top 700 m of the water column, again suggesting a greater level of mixing whenever HF forcings are used. Temperature differences between the three runs in regions characterized the presence of internal waves generated by the mean flow over rough topography are much reduced (not shown).

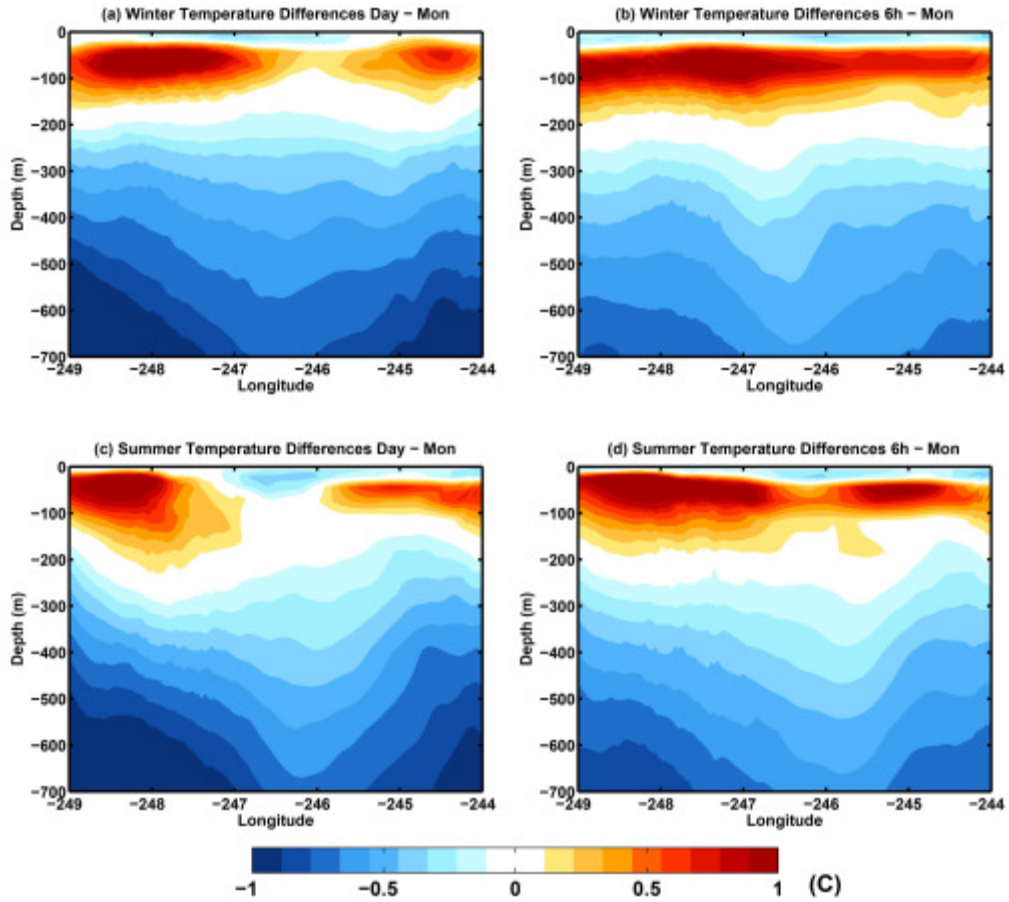

Figure 4. Mean temperature differences in ºC between Day-Day and Mon-Mon (left panels) and 6h-6h and Mon-Mon (right panels), over the top 700 m of the water column along the section shown in black in Figure 5. (a) - (b): boreal winter (DJF); (c) - (d) Summer (JJA).

In the sensitivity integrations, where heat fluxes are varied but 6-hourly winds are used in all three runs, the modeled temperature profiles are indistinguishable for all seasons (Figure 4 bottom panels). This confirms that in the SCS HF winds are responsible for the modeled enhanced vertical mixing, while the frequency of the heat fluxes does not contribute substantially. This is not a generic result, but specific to the SCS and is related to its latitude, given that the variability of the heat fluxes is somehow limited in the tropics, and to the eddy formation mechanism. In conclusions, the principal factor that modifies the mixed layer depth in the SCS is

the wind stress, and minor differences are attributable to the net heat and fresh water fluxes, in agreement with the findings of Fan et al., (2010).

CHAPTER 4. HIGH FREQUENCY WINDS AND THE HORIZONTAL FLOW

The horizontal circulation in the SCS is characterized by a vigorous eddy field generated in large part by the interaction of the mean currents with the topographic features in the basin. Figure 5 shows snapshots of the relative vorticity and horizontal velocity fields at the surface and at 1000 m depth. Both cyclonic and anticyclonic eddies, often found in pairs, contribute to the mesoscale field, and are surrounded by strong vorticity filaments. At the depth of 1000 m the eddy field is clearly linked to the presence of sea mountains and to the impinging of the boundary currents on the coastal slope.

In the three integrations the use of monthly averaged, daily or 6-hourly momentum and heat fluxes does not modify the averaged vorticity statistics. The level of mesoscale activity (eddy number and strength) is comparable between the simulations, both at the surface and at depth in all runs, with only a slightly smaller number of strong anticyclonic eddies in favor of cyclonic vorticity in Mon-*Mon* compared to the other two cases. Differences are not statistically significant. We quantify the similarities in Figure 6, where we show the probability density functions (PDFs) of relative vorticity calculated averaging over 700 snapshots taken every two hours between January and March 2005 at the ocean surface and at 1000 m depth (left panel).

The PDFs at 1000 m reveal a slight asymmetry in the vorticity distributions, with predominance of cyclonic vorticity at intermediate values and of anticyclonic vorticity in the tails, in correspondence of the strongest eddies. This is relevant to the propagation of energy injected at the surface as anticyclones trap near inertial waves (Kunze, 1985). Other surface quantities, like sea surface temperature (SST), salinity (SSS) and height (SSH) are also

indistinguishable. Figure 6 shows the time series of the surface eddy kinetic energy (EKE) in the three simulations over the whole integration period (right panel). No statistically significant changes are found whenever monthly, daily or 6-hourly atmospheric forcing is used to force the circulation. Both the seasonal cycle and intraseasonal and interannual variability are similar. Point-by-point differences can be ascribed to internal ocean variability.

Overall, the use of HF winds does not substantially modify the horizontal circulation or the level of mesoscale activity in the South China Sea. We stress again that this is not a generic result and it is associated to the eddy generation mechanism in this basin, which is primarily driven by the interaction of the mean currents with the topography. In other regions of the ocean, the formation of mesoscale structures has been directly linked to wind and heat fluxes forcing (see Luo et al., 2011 and Vage et al., 2008 for compelling examples in the Labrador Sea), and different vorticity distributions and higher EKE levels have been modeled when using HF winds in comparison to monthly averaged stress fields (Casella et al., 2011).

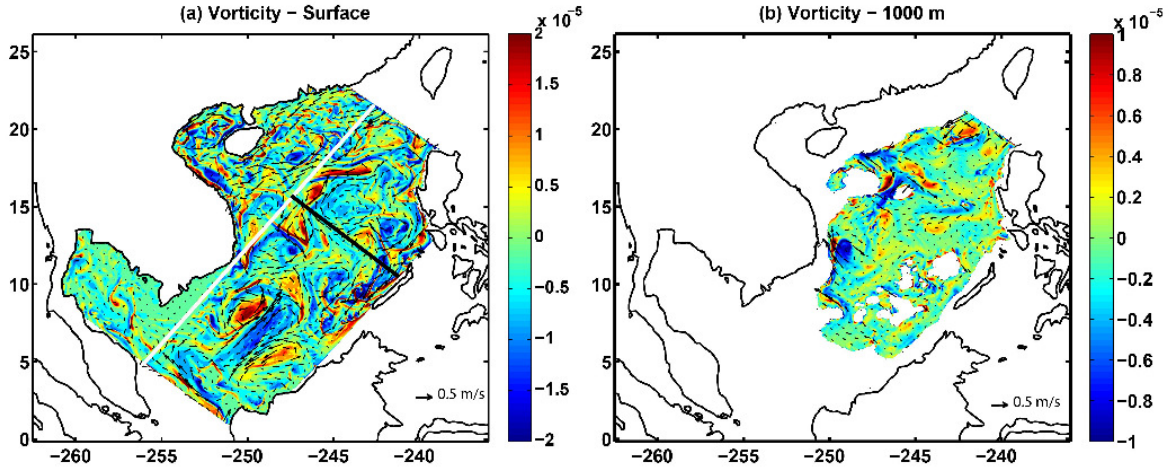

Figure 5. Snapshots of the relative vorticity field (in color) and horizontal velocity (vectors, superimposed) from the Day-Day integration. (a) Surface and (b) 1000 m depth. (Solid lines illustrate the transversal cross-section paths used in analysis. In black the one used in Figure 4; in white the one used in Figure 8)

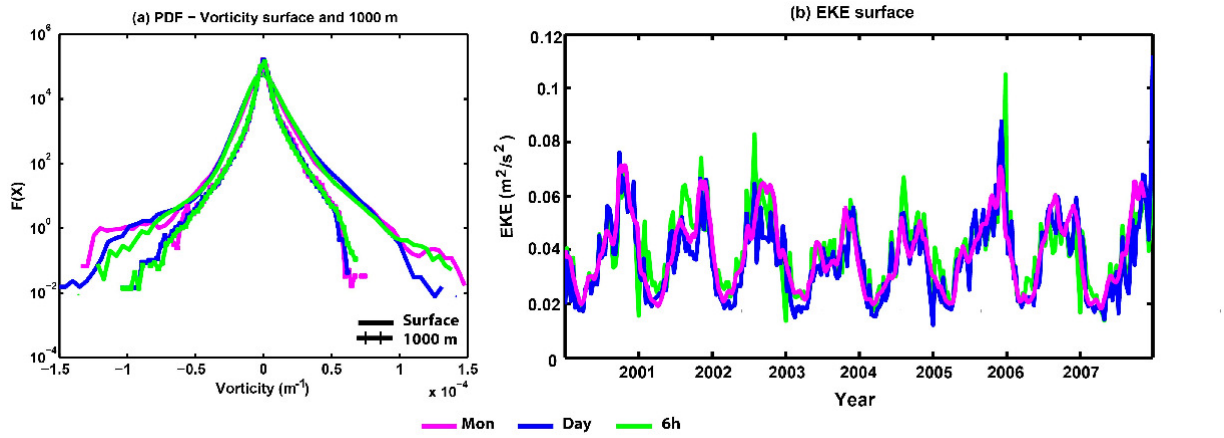

Figure 6. (a) PDF of relative vorticity at the surface and 1000 m. (b) Mean surface eddy kinetic energy time series averaged over whole the domain from 2000 to 2007.

To further quantify the similarity of the horizontal transport properties in the three runs, we calculate the absolute dispersion curves for the Lagrangian particles deployed at 20 and 1000 m depth (see Figure 7). The horizontal absolute dispersion measures the time evolution of the mean square distance in the x-y plane traveled by each particle (i), and it is defined as

$D^2 = \left\langle \left| X_i(t) - X_i(t_0) \right| \right\rangle^2$, where $X_i(t)$ is the (x, y) position of the i-th particle at time t and t_o is the deployment time. Angular brackets indicate average over all the particles released at a given vertical level. All dispersion curves display an analogous behavior, both at the surface and 1000 m, independently of the atmospheric forcing imposed. This further confirms that HF winds (and heat fluxes) do not modify significantly the horizontal circulation in the domain. The dispersion curves scale with a ballistic regime for short time scales (t < 1 day) and display a Brownian behavior after approximately 30 days. This is in agreement with the numerical findings of Koszalka et al., (2009) for an idealized vortex dominated oceanic field and with the analysis of float trajectories in the North Atlantic (e.g. Rupolo et al., 1996).

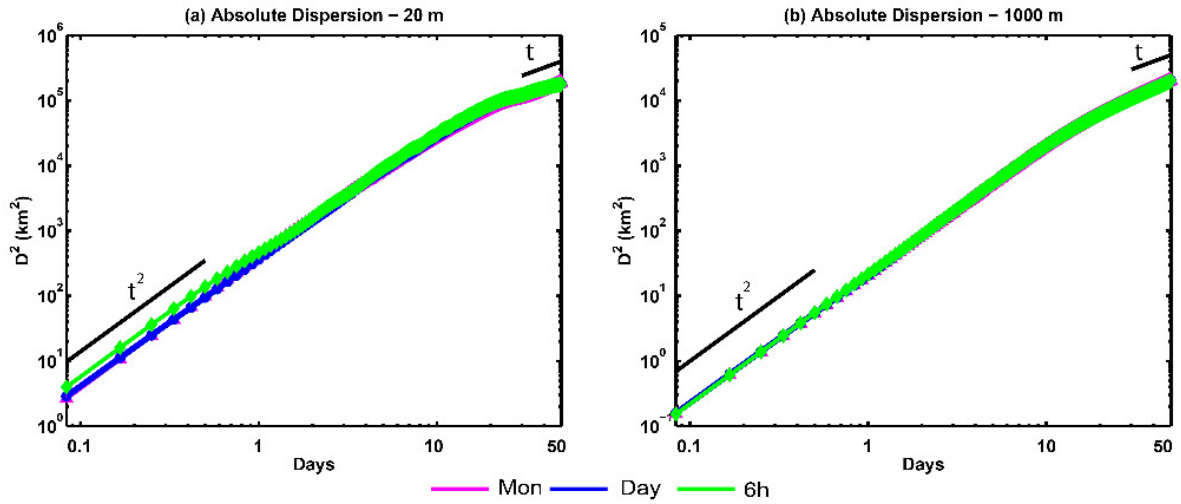

Figure 7. Horizontal absolute dispersion for the Lagrangian tracers deploeyd on Jan 10, 2005 and followed for 50 days for Mon-Mon, Day-Day and 6h-6h. Ballistic and borwnian regimes are also indicated. (a) 20 m and (b) 1000 m.

CHAPTER 5. THE VERTICAL CIRCULATION

The eddy field contributes to the spatially heterogeneity of the vertical mixing at the ocean meso- and submesoscales (Klein et al., 2004; Kunze, 1985; Zhai et al., 2005) and eddies represent localized hotspots of vertical transport (Gill, 1984). Although the level of mesoscale activity identified as number of eddies and intensity of the vorticity fields and the associated horizontal transport are comparable between the three simulations, the vertical velocities show major differences.

Figure 8 displays a south to north transversal section of the instantaneous vertical velocity field in the three integrations (see Figure 5 for its location). In all runs the largest amplitudes are found in association to upward and downward propagating internal waves generated by mean flow motion over the rough bottom. Over intricate bathymetry (between 14 ºN to 17º N in the section shown here), the inertial waves are consistent in both strength and location in all cases evaluated. Where the bathymetry roughness is negligible, on the other hand, the frequency of the atmospheric forcing influences the magnitude and spatial distribution of the vertical velocities. When the domain is forced by monthly winds, the vertical velocities over flat bathymetry are extremely small most of the time; however, in simulations forced by daily and six-hourly winds and heat fluxes, the magnitude of the vertical velocities is several times larger than for monthly winds throughout the water column. The set-up of the numerical experiments suggests that the temporal resolution of the atmospheric forcing field is responsible for the significant increase in vertical velocities, in agreement with previous studies (Danioux et al., 2008; Komori et al., 2008).

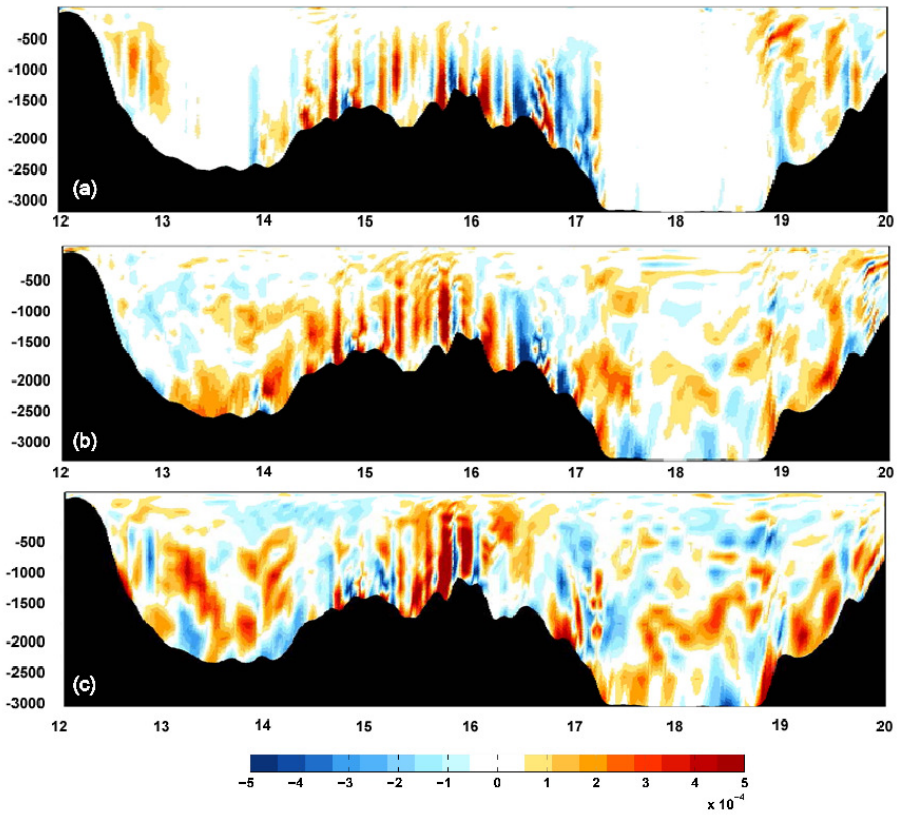

Figure 8. Snapshots of the instantaneous verticial velocity field in m/s over the section indicated in white in Figure 5. Top to Bottom: (a) Mon-Mon, (b) Day-Day and (c) 6h-6h simulations.

In order to quantity the differences in the magnitude in the three simulations we calculate the root mean square (rms) of the horizontally-averaged vertical velocities (Figure 9). We select four sub-domains where the bottom is flat and therefore the interaction of the mean flow and the bathymetry does not contribute to the vertical velocity field, and one where inertial waves over the topographic relief dominate it. Over the flat bottom regions, the magnitude of the rms increases by a factor of six between Mon-*Mon* and Day-*Day* and by almost a factor of two between Day-*Day* and 6h-*6h*, despite the fact that the inertial frequency at this latitude is resolved in the Day-*Day* run. In the monthly profile the rms below the mixed layer remains constant throughout the water column with an average value of 0.2×10^{-4} m/s. In contrast, the daily and 6h profiles show a continuous increase until about 600-700 m before settling until

approximately 2000 m depth at 1.2×10^{-4} and 2.2×10^{-4} m/s, respectively. A slight increase in the rms of the vertical velocities is observed below 2000 m in all integrations, but it is more evident for increasing frequency of the atmospheric forcing. Over steep topography, on the other hand, differences are less pronounced. Vertical velocities are consistently stronger in all runs, and the rms in 6h-*6h* is only twice the one in Mon-*Mon*.

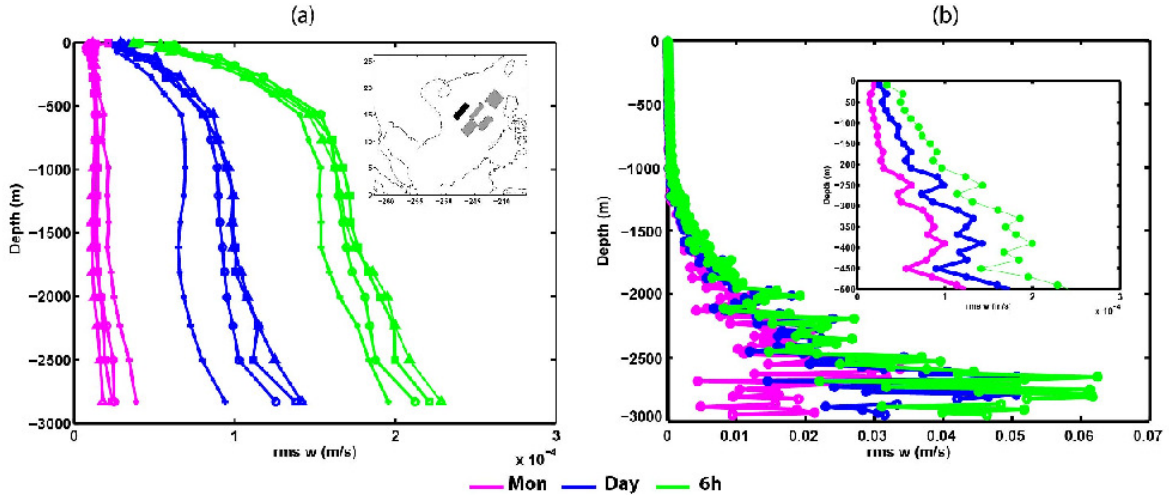

Figure 9. Vertical profile of the rms fluctuations of the vertical velocity (a) averaged over four subdomains where the roughness of the bottom is negligible (gray rectangles in the inset of panel (a)) and (b) averaged over a subdomain characterized by intrincated bathymethy and topographic internal waves (black rectangle in the inset in panel (a)) with a zoom over the first 500 m.

The analysis of the time evolution of the vertical velocity fluctuations points to near inertial waves associated to the mesoscale field as main responsible for the large amplitudes seen in Day-*Day* and 6h-*6h* over flat topography. Evidence is provided in Figure 10, where the frequency spectra for the vertical velocity field are shown for various depths averaged over the regions characterized by a flat bathymetry and by the passage of numerous eddies shown in the inset in Figure 9. There is a noticeable difference between the frequency spectra for the monthly, daily and 6-hourly run in the amplitude of a peak centered at 0.02 cph, which is enhanced for

increasing wind frequency. The peak is more prominent as depth increases and its position is very close to the inertial frequency of 0.022 cph in the South China Sea, in agreement with the theoretical studies by Danoiux and Klein (2008) and Danoiux et al., (2008), the idealized numerical investigation by Koszalka et al. (2009, 2010) and the analysis of a coupled general circulation model run at very high resolution by Komori et al., (2008).

The difference in the spatial distribution of the vertical velocity field between monthly, daily and 6-hourly simulations also points to the eddy field as responsible from trapping the quasi- and near-inertial energy and transporting it through the water column. This can be seen in the vertical velocity field associated with a mesoscale dipole shown for the three simulations in Figure 11. All dipoles form in winter due to the interaction of the main coastal current with the topographic step at about (248 W, 14 ºN), close to Troung Sa Islands, and they propagate into a region of flat bathymetry, where the relative vorticity snapshots are taken (left panels). At the surface positive and negative vorticity defines the mesoscale field. The associated vertical velocity patterns close to the surface (6 m depth; middle panels) illustrate how the mesoscale eddies confine and transport the energy from the atmospheric forcing fields to the ocean, affecting the magnitude and spatial distribution of the vertical velocity field. In both Day-*Day* and 6h-*6h*, vertical velocities in the first 40-50 meters exhibit a spiraling pattern, barely noticeable in Mon-*Mon* and particularly marked in correspondence of the anticyclonic eddy. Those bands have been described in previous works as outward-propagating vortex Rossby-waves (Graves et al., 2006; Koszalka et al., 2009, 2010; McWilliams et al., 2003; Montgomery and Kallenbach, 1997). The VRW frequency in SCS, calculated following Montgomery and Kallenbach (1997), has a period varying between 20 to 40 days depending on the size of the vortices, and it is partially resolved also in the Mon-*Mon* integration.

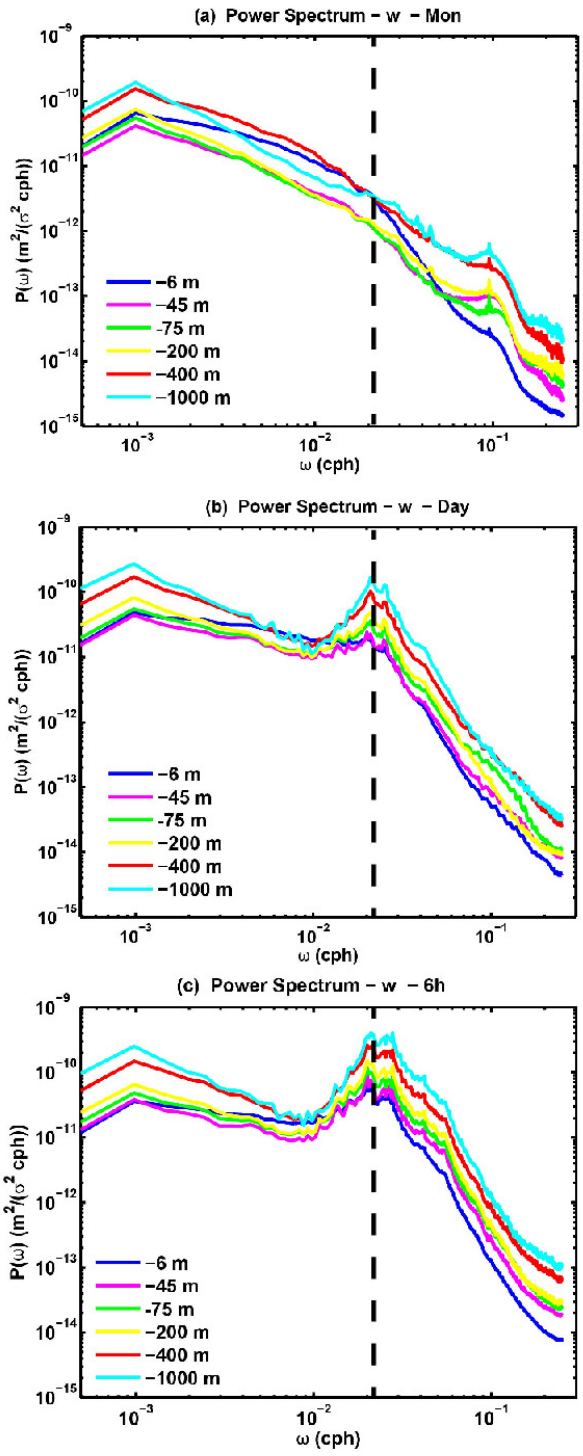

Figure 10. Power spectra of the vertical velocities at 8 m, 45 m, 75 m, 200 m, 400 m and 1000 m depth. Top to Bottomt: Mon-Mon, Day-Day and 6h-6h simulation. In all panles the dash line indicates the inertial frequency in the SCS.

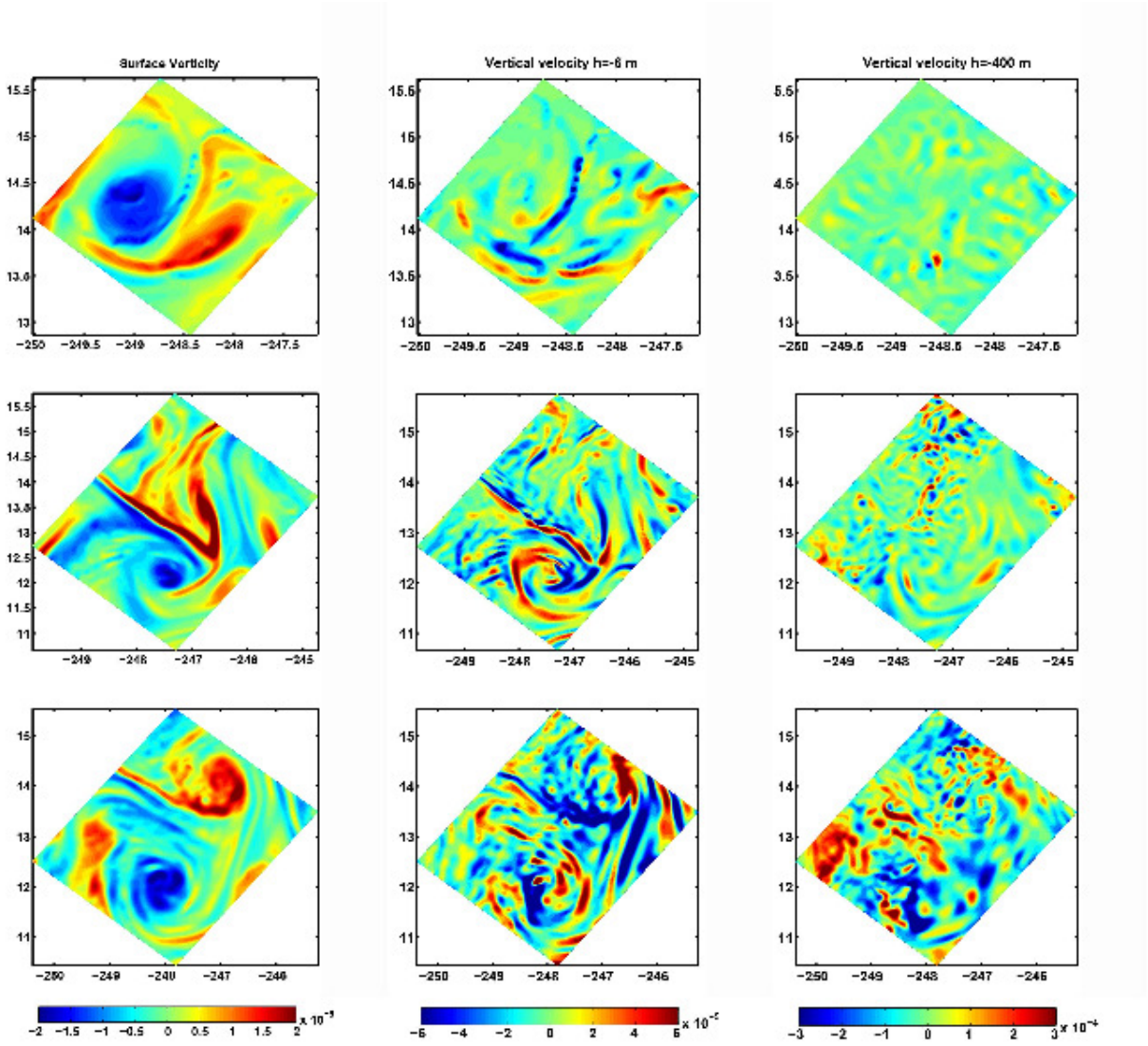

Figure 11. Snapshots of a mesoscale dipole in the SCS in the Mon-Mon (top), Day-Day (middle) and 6h-6h (bottom) simulations. Left to righ: Surface vorticiy (m/s2), vertical velocity (m/s) at 6 m depth and vertical velocity at 400 m depth.

Using a weakly-nonlinear shallow-water model, Graves et al., (2006) demonstrated that in the vortex relaxation process VRWs lead to a weakening of cyclones and a strengthening and reaxisymmetrization of perturbed anticyclones. This causes the slight asymmetry in the vorticity PDFs seen at depth (Figure 6). In other words, cyclonic vortices, formed at the surface by the interaction of the main currents with the bathymetry at a rate analogous to anticyclones, are more

prone to weakening by VRWs. The overall spiraling shape of the vertical velocity field within and around the vortices is determined by the tilting term in the diagnostic equation for the vertical velocity (see Koszalka et al., 2009, 2010 for its mathematical expression). Below the first fifty meters the tilting term becomes negligible compared to the ageostrophic term in the diagnostic equation for the vertical velocity and near inertial waves dominate the vertical velocity field, as seen also in the frequency spectra, again in agreement with the analysis by Koszalka et al., (2009) for an idealized eddy field. Differences between Mon-*Mon* and Day-*Day* and 6h-*6h* raise below the first few hundred of the water column: The energy injected by the winds into the eddies vanishes at such depth in the simulation forced by monthly fields, and but reaches the bottom for the daily and 6-hourly runs. The impact of HF winds on the vertical transport is further evaluated using the Lagrangian trajectories. The signature of quasi- and near-inertial oscillations signature is evident in the vertical projections of the tracer trajectories. Figure 12 shows the vertical excursion that a sample particle deployed at 20 m (panel a) and at 1000 m (panel b) depth undergoes when the circulation is forced by monthly, daily and 6-hourly atmospheric forcing. Particles in Day-Day and 6h-6h runs display an oscillatory motion due to presence of the near-inertial waves. Close to the surface the impact of a VRW is detectable in the case of daily forcing for the whole 50 days and in the case of 6-hourly forcing for the first 20, after which the particle is expelled by the vortex core. The particle-averaged vertical excursion is quantified by the PDFs of the displacements (Figure 12, panels c-d) and the weight of the tails indicates a larger vertical transport for the particles associated with 6-hourly and daily forcing than in Mon-*Mon*, particularly for particles released at 20m. VRWs dominate the vertical velocity structure at those depths and are responsible for the enhanced transport.

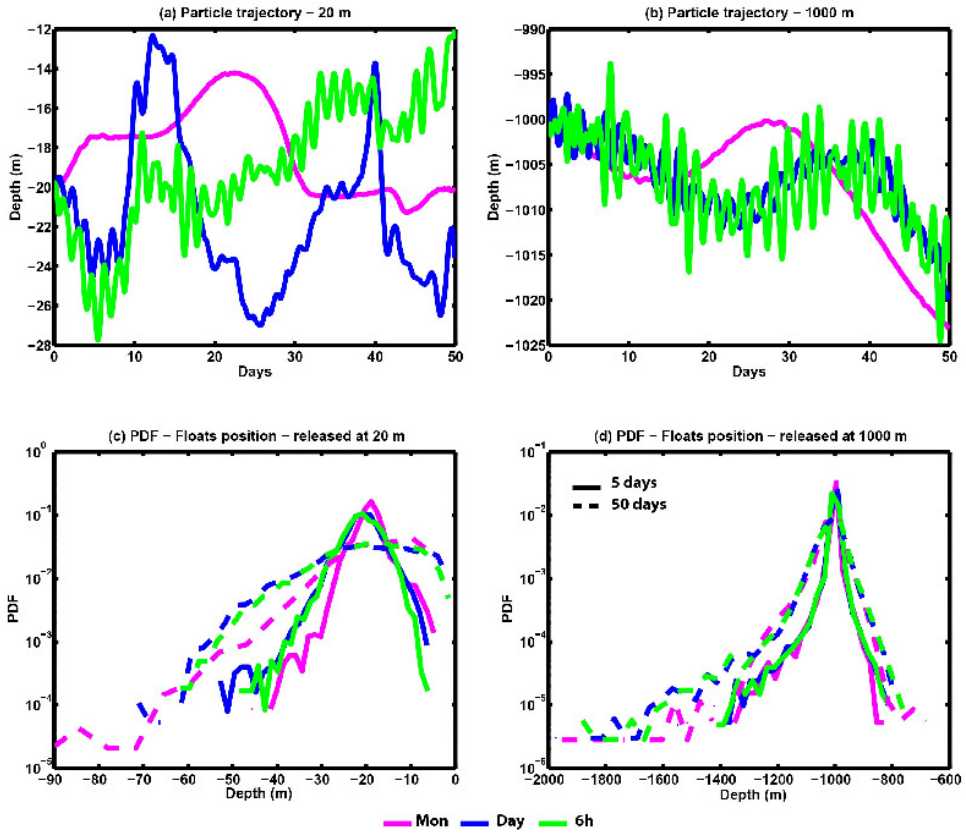

Figure 12. (a)-(b)Samples of single particle trajectories in the Mon-Mon, Day-Day and 6h-6h runs and (c)-(d) PDFs of particle vertical displacement after 5 (solid lines) and 50 (dashed line) days for particles released at 20 m (a and c), and particles released at 1000 m (b-d).

Differences in the PDFs between the three runs are larger close to the surface and in the first 5-10 days, and decrease thereafter. This is due to the fact that near-inertial waves contribute effectively to small displacements, that are averaged out over few inertial periods. Additionally, particles spread over regions where the inertial motions generated by rough topography enhance the vertical mixing for all cases. For the first few days after deployment, on the other hand, the vertical transport is due predominantly to the mesoscale structures and it is significantly greater in the 6h-*6h* and Day-*Day* runs than when monthly winds force the circulation.

CHAPTER 6. CONCLUDING REMARKS

In this work we investigated the impact of high frequency atmospheric forcing in simulating the mesoscale transport in the South China Sea. The SCS is characterized by an intense eddy field generated primarily by the interaction of the local currents with the complex bathymetry. We confirm that the temporal scale variation from monthly to 6-hourly in the wind forcing impacts the circulation far more substantially than an analogous variation in the heat fluxes. Additionally, the frequency of the forcing products does not affect the horizontal dynamics and transport. Variables as sea surface height, horizontal velocities, relative vorticity and eddy kinetic energy at all levels, do not exhibit significant differences. Lagrangian tracers deployed close to the surface and at depth are characterized by analogous horizontal dispersion curves. This is not a generic result, but specific to the SCS and, likely, to all regions where the generation of the eddy field is controlled by the topography. The eddy generation mechanism determines the relative role of high frequency atmospheric forcing on the horizontal properties of the flow, contributing to the complexity of the problem of parameterizing quasi- and near-inertial processes at the mesoscale.

HF winds, on the other hand, impact the representation of the vertical transport that gets stronger as the temporal resolution increases. Whenever the bottom is flat, the magnitude of the vertical velocities associated with the mesoscale eddy field is strongly modified by the wind frequency. Vertical velocity in runs forced by 6-hourly winds are two times greater than when daily averages are used, and twelve times larger than for monthly averaged winds. The doubling seen when replacing daily with 6-hourly winds suggests that resolving the inertial frequency (about 1.9 days for the SCS) is not enough to fully capture the complexity of the inertial and

quasi-inertial wave field with an ocean model and further complicates the representation of vertical mixing at high latitudes, where eddies are abundant and the inertial frequency is only few hours.

The energy injected by the winds into the ocean is transported in the water column by mesoscale eddies via vortex Rossby waves and near inertial oscillations, whenever the wind forcing contains energy at frequencies in the inertial and subinertial bands. In the SCS VRWs, identified here for the first time in a realistic modeling configuration, module the magnitude and spatial distribution of the vertical velocity field with their characteristic spiraling shape in the upper 40-50 meters of the water column, while NI oscillations dominate below the first 50 m. Analyzing the vertical transport properties associated with those two forms of waves, we found that VRWs are more effective at increasing mixing within the upper water column than near inertial waves at depth. In the South China Sea this is evident for particles deployed in regions with flat bathymetry and on time scale of about 2-20 days depending on depth, after which most tracers encounter inertial waves induced by the mean current flowing over the complicated bathymetry independently on the frequency of the atmospheric forcing. This property may have important consequences for the representation of biogeochemical interactions and planktonic activity in the euphotic layer in couple ocean-biogeochemical models.

REFERENCES

Abraham, E.R., 1998. The generation of plankton patchiness by turbulent stirring. Nature 391, 577-580.

Balmaseda, M.A., Vidard, A., Anderson, D.L.T., 2008. The ECMWF Ocean Analysis System: ORA-S3. Monthly Weather Review 136, 3018-3034.

Bracco, A., Clayton, S., Pasquero, C., 2009. Horizontal advection, diffusion, and plankton spectra at the sea surface. J. Geophys. Res. 114, C02001.

Bracco, A., LaCasce, J., Pasquero, C., Provenzale, A., 2000. The velocity distribution of barotropic turbulence. Physics of Fluids 12, 2478.

Bracco, A., McWilliams, J.C., 2010. Reynolds-number dependency in homogeneous, stationary two-dimensional turbulence. Journal of Fluid Mechanics 646, 517-526.

Byun, S.-S., Park, J.J., Chang, K.-I., Schmitt, R.W., 2010. Observation of near-inertial wave reflections within the thermostad layer of an anticyclonic mesoscale eddy. Geophys. Res. Lett. 37, L01606.

Capet, X., McWilliams, J.C., Molemaker, M.J., Shchepetkin, A.F., 2008. Mesoscale to Submesoscale Transition in the California Current System. Part I: Flow Structure, Eddy Flux, and Observational Tests. Journal of Physical Oceanography 38, 29-43.

Carton, J.A., Giese, B.S., 2008. A Reanalysis of Ocean Climate Using Simple Ocean Data Assimilation (SODA). Monthly Weather Review 136, 2999-3017.

Casella, E., Molcard, A., Provenzale, A., Mesoscale vortices in the Ligurian Sea and their effect on coastal upwelling processes. Journal of Marine Systems. doi:10.1016/j.jmarsys.2011.02.019

Chavanne, C.P., Flament, P., Luther, D.S., Gurgel, K.-W., 2010. Observations of Vortex Rossby Waves Associated with a Mesoscale Cyclone. Journal of Physical Oceanography 40, 2333-2340.

Chen, D., Liu, W.T., Zebiak, S.E., Cane, M.A., Kushnir, Y., Witter, D., 1999. Sensitivity of the tropical Pacific Ocean simulation to the temporal and spatial resolution of wind forcing. J. Geophys. Res. 104, 11261-11271.

Chin, T.M., Milliff, R.F., Large, W.G., 1998. Basin-Scale, High-Wavenumber Sea Surface Wind Fields from a Multiresolution Analysis of Scatterometer Data. Journal of Atmospheric and Oceanic Technology 15, 741-763.

Chu, P.C., Li, R., 2000. South China Sea Isopycnal-Surface Circulation. Journal of Physical Oceanography 30, 2419-2438.

Danioux, E., Klein, P., 2008. A Resonance Mechanism Leading to Wind-Forced Motions with a 2f Frequency. Journal of Physical Oceanography 38, 2322-2329.

Danioux, E., Klein, P., Riviere, P., 2008. Propagation of Wind Energy into the Deep Ocean through a Fully Turbulent Mesoscale Eddy Field. Journal of Physical Oceanography 38, 2224-2241.

Ezer, T., 2000. On the seasonal mixed layer simulated by a basin-scale ocean model and the Mellor-Yamada turbulence scheme. J. Geophys. Res. 105, 16843-16855.

Fan, C., Wang, J., Song, J., 2010. Factors influencing the climatological mixed layer depth in the South China Sea: numerical simulations. Chinese Journal of Oceanology and Limnology 28, 1112-1118.

Fang, G., Wei, Z., Choi, B.-H., Wang, K., Fang, Y., Li, W., 2003. Interbasin freshwater, heat and salt transport through the boundaries of the East and South China Seas from a variable-grid global ocean circulation model. Science in China Series D: Earth Sciences 46, 149-161.

Garrett, C., 2003. Internal Tides and Ocean Mixing. Science 301, 1858-1859.

Gill, A.E., 1984. On the Behavior of Internal Waves in the Wakes of Storms. Journal of Physical Oceanography 14, 1129-1151.

Graves, L.P., McWilliams, J.C., Montgomery, M.T., 2006. Vortex evolution due to straining: a mechanism for dominance of strong, interior anticyclones. Geophysical & Astrophysical Fluid Dynamics 100, 151-183.

Hu, J., Kawamura, H., Hong, H., Qi, Y., 2000. A Review on the Currents in the South China Sea: Seasonal Circulation, South China Sea Warm Current and Kuroshio Intrusion. Journal of Oceanography 56, 607-624.

Josey, S.A., 2001. A Comparison of ECMWF, NCEP-NCAR, and SOC Surface Heat Fluxes with Moored Buoy Measurements in the Subduction Region of the Northeast Atlantic. Journal of Climate 14, 1780-1789.

Kamenkovich, I.V., 2005. Role of daily surface forcing in setting the temperature and mixed layer structure of the Southern Ocean. J. Geophys. Res. 110, C07006.

Kara, A.B., Hurlburt, H.E., Wallcraft, A.J., Bourassa, M.A., 2005. Black Sea Mixed Layer Sensitivity to Various Wind and Thermal Forcing Products on Climatological Time Scales*. Journal of Climate 18, 5266-5293.

Kistler, R., Kalnay, E., Collins, W., Saha, S., White, G., Woollen, J., Chelliah, M., Ebisuzaki, W., Kanamitsu, M., Kousky, V., van den Dool, H., Jenne, R., Fiorino, M., 2001. The NCEP-NCAR 50-Year Reanalysis: Monthly Means CD-ROM and Documentation. Bulletin of the American Meteorological Society 82, 247.

Klein, P., Lapeyre, G., 2009. The Oceanic Vertical Pump Induced by Mesoscale and Submesoscale Turbulence. Annual Review of Marine Science 1, 351-375.

Klein, P., Lapeyre, G., Large, W.G., 2004. Wind ringing of the ocean in presence of mesoscale eddies. Geophys. Res. Lett. 31, L15306.

Komori, N., Ohfuchi, W., Taguchi, B., Sasaki, H., Klein, P., 2008. Deep ocean inertia-gravity waves simulated in a high-resolution global coupled atmosphere–ocean GCM. Geophys. Res. Lett. 35, L04610.

Koszalka, I., Bracco, A., McWilliams, J.C., Provenzale, A., 2009. Dynamics of wind-forced coherent anticyclones in the open ocean. J. Geophys. Res. 114, C08011.

Koszalka, I., Ceballos, L., Bracco, A., 2010. Vertical mixing and coherent anticyclones in the ocean: the role of stratification. Nonlin. Processes Geophys. 17, 37-47.

Kundu, P.K., Thomson, R.E., 1985. Inertial Oscillations due to a Moving Front. Journal of Physical Oceanography 15, 1076-1084.

Kunze, E., Sanford, T.B., 1984. Observations of Near-Inertial Waves in a Front. Journal of Physical Oceanography 14, 566-581.

Kunze, E., Sanford, T.B., 1986. Near-Inertial Wave Interactions with Mean Flow and Bottom Topography near Caryn Seamount. Journal of Physical Oceanography 16, 109-120.

Large, W.G., Crawford, G.B., 1995. Observations and Simulations of Upper-Ocean Response to Wind Events during the Ocean Storms Experiment. Journal of Physical Oceanography 25, 2831-2852.

Large, W.G., McWilliams, J.C., Doney, S.C., 1994. Oceanic vertical mixing: A review and a model with a nonlocal boundary layer parameterization. Rev. Geophys. 32, 363-403.

Lau, K.M., Wu, H.T., Yang, S., 1998. Hydrologic Processes Associated with the First Transition of the Asian Summer Monsoon: A Pilot Satellite Study. Bulletin of the American Meteorological Society 79, 1871-1882.

Lee, D.-K., Niiler, P.P., 1998. The inertial chimney: The near-inertial energy drainage from the ocean surface to the deep layer. J. Geophys. Res. 103, 7579-7591.

Lee, T., Liu, W.T., 2005. Effects of high-frequency wind sampling on simulated mixed layer depth and upper ocean temperature. J. Geophys. Res. 110, C05002.

Levy, M., Klein, P., 2004. Does the low frequency variability of mesoscale dynamics explain a part of the phytoplankton and zooplankton spectral variability? Proceedings of the Royal Society of London. Series A: Mathematical, Physical and Engineering Sciences 460, 1673-1687.

Lueck, R., Reid, R., 1984. On the Production and Dissipation of Mechanical Energy in the Ocean. J. Geophys. Res. 89, 3439-3445.

Luo, H., Bracco, A., Di Lorenzo, E., The interannual variability of the surface eddy kinetic energy in the Labrador Sea. Progress In Oceanography. doi:10.1016/j.pocean.2011.01.006.

Macdonald, N.J., 1968. The evidence for the existence of Rossby-like waves in the hurricane vortex. Tellus 20, 138-150.

Marchesiello, P., McWilliams, J.C., Shchepetkin, A., 2001. Open boundary conditions for long-term integration of regional oceanic models. Ocean Modelling 3, 1-20.

Martin, A.P., Richards, K.J., 2001. Mechanisms for vertical nutrient transport within a North Atlantic mesoscale eddy. Deep Sea Research Part II: Topical Studies in Oceanography 48, 757-773.

McGillicuddy, D.J., Robinson, A.R., 1997. Eddy-induced nutrient supply and new production in the Sargasso Sea. Deep Sea Research Part I: Oceanographic Research Papers 44, 1427-1450.

McWilliams, J.C., 1984. The emergence of isolated coherent vortices in turbulent flow. Journal of Fluid Mechanics 146, 21-43.

McWilliams, J.C., 1990. The vortices of two-dimensional turbulence. Journal of Fluid Mechanics 219, 361-385.

McWilliams, J.C., Graves, L.P., Montogomery, M.T., 2003. A Formal Theory for Vortex Rossby Waves and Vortex Evolution. Geophysical & Astrophysical Fluid Dynamics 97, 275.

Metzger, E., 2003. Upper Ocean Sensitivity to Wind Forcing in the South China Sea. Journal of Oceanography 59, 783-798.

Milliff, R.F., Morzel, J., Chelton, D.B., Freilich, M.H., 2004. Wind Stress Curl and Wind Stress Divergence Biases from Rain Effects on QSCAT Surface Wind Retrievals. Journal of Atmospheric and Oceanic Technology 21, 1216-1231.

Montgomery, M.T., Kallenbach, R.J., 1997. A theory for vortex rossby-waves and its application to spiral bands and intensity changes in hurricanes. Quarterly Journal of the Royal Meteorological Society 123, 435-465.

Munk, W., Wunsch, C., 1998. Abyssal recipes II: energetics of tidal and wind mixing. Deep Sea Research Part I: Oceanographic Research Papers 45, 1977-2010.

Pasquero, C., Bracco, A., Provenzale, Weiss, J.B., 2007. Particle motion in the sea of eddies, Lagrangian Analysis and Prediction of Coastal and Ocean Dynamics. Cambridge University Press, pp. 89-118.

Pasquero, C., Bracco, A., Provenzale, A., 2005. Impact of the spatiotemporal variability of the nutrient flux on primary productivity in the ocean. J. Geophys. Res. 110, C07005.

Pollard, R.T., Millard Jr, R.C., 1970. Comparison between observed and simulated wind-generated inertial oscillations. Deep Sea Research and Oceanographic Abstracts 17, 813-816, IN815, 817-821.

Provenzale, A., 1999. Transport by coherent barotropic vortices. Annual Review of Fluid Mechanics 31, 55.

Qu, T., 2000. Upper-Layer Circulation in the South China Sea. Journal of Physical Oceanography 30, 1450-1460.

Rabinovich, A., Thomson, R., Bograd, S., 2002. Drifter Observations of Anticyclonic Eddies near Bussol' Strait, the Kuril Islands. Journal of Oceanography 58, 661-671.

Rogachev, K., Carmack, E., 2002. Evidence for the Trapping and Amplification of Near-Inertial Motions in a Large Anticyclonic Ring in the Oyashio. Journal of Oceanography 58, 673-682.

Rupolo, V., Artale, V., Hua, B.L., Provenzale, A., 1996. Lagrangian Velocity Spectra at 700 m in the Western North Atlantic. Journal of Physical Oceanography 26, 1591-1607.

Shchepetkin, A.F., McWilliams, J.C., 1998. Quasi-Monotone Advection Schemes Based on Explicit Locally Adaptive Dissipation. Monthly Weather Review 126, 1541-1580.

Shchepetkin, A.F., McWilliams, J.C., 2005. The regional oceanic modeling system (ROMS): a split-explicit, free-surface, topography-following-coordinate oceanic model. Ocean Modelling 9, 347-404.

Skyllingstad, E.D., Smyth, W.D., Crawford, G.B., 2000. Resonant Wind-Driven Mixing in the Ocean Boundary Layer. Journal of Physical Oceanography 30, 1866-1890.

Smith, T.M., Reynolds, R.W., 2003. Extended Reconstruction of Global Sea Surface Temperatures Based on COADS Data (1854-1997). Journal of Climate 16, 1495-1510.

Stammer, D., 1997. Global Characteristics of Ocean Variability Estimated from Regional TOPEX/POSEIDON Altimeter Measurements. Journal of Physical Oceanography 27, 1743-1769.

Sui, C.-H., Li, X., Rienecker, M.M., Lau, K.-M., Laszlo, I., Pinker, R.T., 2003. The Role of Daily Surface Forcing in the Upper Ocean over the Tropical Pacific: A Numerical Study. Journal of Climate 16, 756-766.

Vage, K., Pickart, R.S., Moore, G.W.K., Ribergaard, M.H., 2008. Winter Mixed Layer Development in the Central Irminger Sea: The Effect of Strong, Intermittent Wind Events. Journal of Physical Oceanography 38, 541-565.

Wang, G., Chen, D., Su, J., 2006. Generation and life cycle of the dipole in the South China Sea summer circulation. J. Geophys. Res. 111, C06002.

Wei, Z., Fang, G., Choi, B.-H., Fang, Y., He, Y., 2003. Sea surface height and transport stream function of the South China Sea from a variable-grid global ocean circulation model. Science in China Series D: Earth Sciences 46, 139-148.

Wu, C.-R., Shaw, P.-T., Chao, S.-Y., 1998. Seasonal and interannual variations in the velocity field of the South China Sea. Journal of Oceanography 54, 361-372.

Wunsch, C., Ferrari, R., 2004. Vertical mixing, energy, and the general circulation of the oceans. Annual Review of Fluid Mechanics 36, 281-314.

Wyrtki, K., 1961. Scientific results of marine investigations of the South China Sea and the Gulf of Thailand, 1959-1961 in: University of California, S.I.o.O. (Ed.). University of California, Scripps Institution of Oceanography, La Jolla.

Xue, H., Chai, F., Pettigrew, N., Xu, D., Shi, M., Xu, J., 2004. Kuroshio intrusion and the circulation in the South China Sea. J. Geophys. Res. 109, C02017.

Zhai, X., Greatbatch, R.J., Eden, C., 2007. Spreading of near-inertial energy in a 1/12° model of the North Atlantic Ocean. Geophys. Res. Lett. 34, L10609.

Zhai, X., Greatbatch, R.J., Zhao, J., 2005. Enhanced vertical propagation of storm-induced near-inertial energy in an eddying ocean channel model. Geophys. Res. Lett. 32, L18602.